Inorg. Chem. **2003**, *42*, 1121–1129

Inorganic Chemistry
Article

Mixed Valence in $YBaFe_2O_5$

Patrick M. Woodward[†] **and Pavel Karen***

Department of Chemistry, The Ohio State University, 100 West 18th Avenue,
Columbus, Ohio 43210-1185, and Department of Chemistry, University of Oslo,
POB1033 Blindern, N-0315, Norway

Received September 11, 2002

$YBaFe_2O_5$ has been synthesized by heating a nanoscale citrate precursor in a carefully controlled reducing environment. Successful synthesis of a single-phase sample can only be achieved in a narrow window of oxygen partial pressures and temperatures. $YBaFe_2O_5$ adopts an oxygen-deficient perovskite-type structure, which contains double layers of corner sharing FeO_5 square pyramids separated by Y^{3+} ions. At $T_N \cong 430$ K, tetragonal (*P*4/*mmm*) and paramagnetic $YBaFe_2O_5$ orders antiferromagnetically (AFM) experiencing a slight orthorhombic distortion (*Pmmm*). Around this temperature, it can be characterized as a class-III mixed valence (MV) compound, where all iron atoms exist as equivalent MV $Fe^{2.5+}$ ions. The magnetic structure is characterized by AFM Fe–O–Fe superexchange coupling within the double layers and a ferromagnetic Fe–Fe direct-exchange coupling between neighboring double layers. Upon cooling below ∼335 K, a premonitory charge ordering ($2Fe^{2.5+} \rightarrow Fe^{2.5+\delta} + Fe^{2.5-\delta}$) into a class-II MV phase takes place. This transition is detected by differential scanning calorimetry, but powder diffraction techniques fail to detect any volume change or a long-range structural order. At ∼308 K, a complete charge ordering ($2Fe^{2.5+} \rightarrow Fe^{2+} + Fe^{3+}$) into a class-I MV compound takes place. This charge localization triggers a number of changes in the crystal, magnetic, and electronic structure of $YBaFe_2O_5$. The magnetic structure rearranges to a G-type AFM structure, where both the Fe–O–Fe superexchange and the Fe–Fe direct-exchange couplings are antiferromagnetic. The crystal structure rearranges (*Pmma*) to accommodate alternating chains of Fe^{2+} and Fe^{3+} running along *b* and an unexpectedly large cooperative Jahn–Teller distortion about the high-spin Fe^{2+} ions. This order of charges does not fulfill the Anderson condition, and it rather corresponds to an ordering of doubly occupied Fe^{2+} d_{xz} orbitals. Comparisons with $YBaMn_2O_5$ and $YBaCo_2O_5$ are made to highlight the impact of changing the d-electron count.

Introduction

Mixed valence (MV), Jahn–Teller distortions, and magnetic ordering are topics that have long interested inorganic chemists. Classical examples of MV in extended inorganic solids include cases so diverse as the pigments minium (Pb_3O_4) and Prussian blue on the one side and tungsten bronzes, high-T_c superconductors, and magnetite on the other side. These compounds have been widely studied for their interesting optical, electrical, and magnetic properties. Day and Robin classified MV compounds into three different classes.[1] Class-I MV compounds are characterized by very different coordination environments for the ions of each oxidation state. They contain localized electrons and exhibit insulating behavior. Class-II MV compounds also have different environments for ions of differing oxidation states, but the sites are sufficiently similar so that electron transfer can occur with only a small input of energy. Class-III MV compounds contain delocalized electrons so that all of the MV atoms have the same chemical environment and the same oxidation state. Of particular interest are compounds that transform from either class-III or class-II MV to class-I MV upon cooling. This type of transition, triggered by electron localization, is often referred to as charge ordering.

The Jahn–Teller theorem states that a nonlinear molecule in an electronically degenerate state must undergo a distortion in order to remove the degeneracy, thereby lowering both the symmetry and the energy of the molecule.[2] In an extended solid, where the polyhedra are linked to form a three-dimensional bond network, the Jahn–Teller distortion that occurs at each polyhedron is felt by the neighboring

---

* Corresponding author. E-mail: pavel.karen@kjemi.uio.no. Office phone: +47 228 555 90.

[†] E-mail: woodward@chemistry.ohio-state.edu.

(1) Robin, M. B.; Day, P. *Adv. Inorg. Chem. Radiochem.* **1967**, *10*, 247.

(2) Jahn, H. A.; Teller, E. *Proc. R. Soc. London* **1937**, *A161*, 220.

10.1021/ic026022z CCC: $25.00

polyhedra. Consequently, the direction and size of the distortions must be cooperative throughout the crystal. Goodenough was among the first to recognize this fact during studies of the structural and magnetic properties of $La_{1-x}Ca_xMnO_3$ perovskites.[3] These studies led him to coin the term cooperative Jahn–Teller distortion (CJTD) to describe this phenomenon. More recently, the term orbital ordering has come into vogue to describe preferential occupation of lower energy d-orbitals, which is of course the driving force behind a CJTD. This same pioneering work was also important in the development of the Goodenough–Kanamori superexchange rules,[4] which are widely used to understand magnetic ordering in extended solids. Because both CJTD and magnetic ordering are sensitive to changes in the filling of the d-orbitals, charge-ordering transitions should in principle be strongly coupled with both orbital and magnetic ordering transitions. Nonetheless, there are relatively few documented examples of compounds where all three transitions, viz., charge ordering, orbital ordering, and spin rearrangement, occur simultaneously. One such example is $NdSrMn_2O_6$, which transforms upon cooling from a ferromagnetic (FM), class-III MV metal into an antiferromagnetic (AFM), orbitally ordered, class-I MV insulator.[5]

The oldest and most studied example of charge ordering is the Verwey transition in magnetite.[6] Magnetite undergoes a phase transition at 124 K[7] to stabilize an ordered arrangement of Fe^{2+} and Fe^{3+} on the octahedral sites of the spinel structure. The details of the complex crystal structure of the low-temperature charge-ordered phase have remained a challenge for more than 60 years.[8] Double-cell perovskites $RBaFe_2O_5$ (R = trivalent rare-earth ion) are the most recent contribution to the family of compounds that exhibit a Verwey transition.[9] The half-integer oxidation state of iron and the corner sharing square-pyramidal framework of the double-cell perovskite structure set the stage for a charge-ordering transition whose structural evolution can be accurately characterized on both sides of the transition. At high temperatures, Mössbauer spectroscopy,[9,10] as well as synchrotron and neutron powder diffraction,[9,11] detects a single iron site occupied by an $Fe^{2.5+}$ ion, characteristic of a class-III MV compound. Upon cooling, previous studies reveal a two-step charge-ordering process. First, a premonitory transition occurs, which gives rise to two different iron signals, $Fe^{2.5+\delta}$ and $Fe^{2.5-\delta}$, in the Mössbauer data. This intermediate region is best described as a class-II MV state. Further cooling below the Verwey temperature (T_V) completes the transition into a class-I MV state, characterized by equal concentrations of Fe^{2+} and Fe^{3+}. The latter transition can be detected and characterized by diffraction methods, which reveal a three-dimensional charge-ordered arrangement of the two ions, as well as a pronounced change in the unit-cell dimensions and a rearrangement of the magnetic structure.[9] Consequently, these compounds provide an unusual opportunity to study a MV transition that triggers both a cooperative Jahn–Teller distortion and a magnetic phase transition.

Previous studies on double-cell perovskites $RBaFe_2O_5$ have been carried out for R = Tb,[9] Nd, and Sm.[10,11] These studies have shown that the details of the phase transitions are very sensitive to changes in the size of the rare-earth ion. This paper describes the synthesis and characterization of another member of this family, $YBaFe_2O_5$. Neutron powder diffraction and differential scanning calorimetry are used to track the structural and magnetic phase transitions of this compound. Electronic structure calculations are utilized to estimate the crystal field splitting associated with the square-pyramidal coordination of iron, and to understand how the Jahn–Teller distortions alter this crystal field splitting. Among the double-cell perovskites containing iron, $YBaFe_2O_5$ is of particular interest because charge ordering has also been reported in $YBaMn_2O_5$[12] and $YBaCo_2O_5$.[13] Those results combined with this study allow for a direct comparison of how changes in the d-orbital population influence the stability of various combinations of charge, orbital, and magnetic ordering.

Experimental Section

Synthesis and Compositional Characterization. The master sample of $YBaFe_2O_{5+w}$ was synthesized from nanoscale precursors obtained by liquid mixing in a citrate melt. Standardized Y_2O_3 (99.99% Fluka) was dry-mixed with high-purity citric acid monohydrate (Fluka, <0.02% sulfate ash) in a 1:40 molar ratio. This mixture was dissolved upon melting assisted by a small amount of water. Iron (lumps, 99.95% Koch-Light) was dissolved in dilute HNO_3 and gradually added into the melt, while the mixture was warmed until nitrous gases nearly ceased to develop. After cooling below 100 °C, redistilled water was added, and barium carbonate (Fluka, <0.2% Sr) was dissolved into the reaction mixture. The resulting clear viscous melt was decomposed into an organic-based solid at 180 °C, homogenized in a vibration mill, and incinerated for 5 days in a covered porcelain crucible at 400 °C. At this stage, the reaction mixture was an amorphous nanoscale precursor, as confirmed by X-ray diffraction. The precursor was then (a) calcined at 860 °C, (b) pressed into cylinders (150 kg/cm^2), (c) sintered at 1020 °C, and (d) annealed for 7 days at 600 °C to achieve the desired oxygen stoichiometry. The oxygen nonstoichiometry was controlled by high-temperature equilibration and quenching in atmospheres of hydrogen, water, and argon. A mixture of high-purity argon and hydrogen gas with a specific content of water vapor (measured by an Endress–Hauser MMY150 hygrometer) defining a suitable partial pressure of oxygen was applied as the

---

(3) Goodenough, J. B. *Phys. Rev.* **1955**, *100*, 564.

(4) Goodenough, J. B. *Magnetism and the Chemical Bond*; Interscience & Wiley: New York, 1963.

(5) Woodward, P. M.; Cox, D. E.; Vogt, T.; Rao, C. N. R.; Cheetham, A. K. *Chem. Mater.* **1999**, *11*, 3528. Kuwahara, H.; Tomioka, Y.; Asamitsu, A.; Moritomo, Y.; Tokura, Y. *Science* **1995**, *270*, 961.

(6) Verwey, E. J. W. *Nature (London)* **1939**, *144*, 327.

(7) Takai, S.; Akishige, Y.; Kawaji, H.; Atake, T. Sawaguchi, E. *J. Chem. Thermodyn.* **1994**, *26*, 1259.

(8) Wright, J. P.; Attfield, J. P.; Radaelli, P. G. *Phys. Rev. Lett.* **2001**, *87*, 266401.

(9) Karen, P.; Woodward, P. M.; Lindén, J.; Vogt, T.; Studer, A.; Fisher, P. *Phys. Rev. B* **2001**, *64*, 214405.

(10) Lindén, J.; Karen, P.; Kjekshus, A.; Miettinen, J.; Pietari, T.; Karppinen, M. *Phys. Rev. B* **1999**, *60*, 15251.

(11) Karen, P.; Woodward, P. M.; Santhosh, P. N.; Vogt, T.; Stephens, P. W.; Pagola, S. *J. Solid State Chem.* **2002**, *167*, 480.

(12) Millange, F.; Caignaert, V.; Suard, E.; Raveau, B. *Mater. Res. Bull.* **1999**, *34*, 1.

(13) Vogt, T.; Woodward, P. M.; Karen, P.; Hunter, B. A.; Henning, P.; Moodenbaugh, A. R. *Phys. Rev. Lett.* **2000**, *84*, 2969.

Table 1. Synthesis and Characterization of $YBaFe_2O_5$ and Observed Conditions of Redox Instability

	T, °C	Ar/H_2[a]	log(pH_2O), bar	log(pO_2), bar	time, days	a, Å	b, Å	c, Å
calcination	860	112(1)	−1.685(5)	−16.16(2)	1			
sintering	1020	114(2)	−1.71(3)	−14.84(4)	2	4.0074(7)	3.8560(5)	7.556(1)
oxygen-content control	600	21.57(4)	−4.00(5)	−29.00(5)	7	4.0092(4)	3.8551(3)	7.5553(5)
decomposed upon oxidation	1000	123(3)	−1.70(2)	−13.63(1)	4	$YFeO_3$ and $(Y,Ba)FeO_{3-\delta}$		
decomposed upon reduction	1000	9(0)	−1.62(1)	−15.66(2)	5	a green Fe^{2+} product		

[a] Ratio Ar/H_2 is by volume, and standard deviations refer to its variations over the duration of the heating cycle.

reaction atmosphere. The equilibrated bulk sample (5 pellets of about 10 g total) was quenched by a free fall into a metal container filled with high purity Ar (<2 ppm O_2, dried over a P_2O_5 desiccant). A thin surface layer was removed from the sample pellets before further characterizations, and the sample was stored under argon. Details of the conditions employed during each heating cycle are given in Table 1.

Double-cell perovskites are well documented to accommodate oxygen nonstoichiometry of the $RBaM_2O_{5+w}$ type through insertion of excess oxygen into the rare-earth layer. For the bulk sample prepared for this study, the oxygen content was determined by cerimetric titration to be $w = 0.001$. Details of such analyses are in ref 14. In a similar fashion, several small-scale (∼1 g) samples were synthesized with the oxygen content varying closely around $w = 0$, to assess the effect of the oxygen nonstoichiometry on the stability of the phase. For all samples synthesized, the phase purity and unit-cell parameters were evaluated from powder X-ray diffraction data obtained with a focusing Guinier−Hägg camera (Cu Kα_1 radiation using Si as an internal standard). The photographs were scanned by an LS-18 (Nicolet) film scanner with software for X-ray data treatment.[15]

Differential Scanning Calorimetry (DSC). A liquid-nitrogen operated Perkin−Elmer Pyris 1 instrument was used to monitor thermal-flux curves upon heating (10 K/min) between 200 and 380 K. Aluminum pans (50 μL, 50 mg) were used to seal the coarsely powdered samples of 20−60 mg weight. Peak temperatures were corrected to zero sample-weight on the basis of a separate calibration series. The temperature scale was calibrated on cyclopentane, cyclohexane, *n*-octane, *n*-decane, *n*-dodecane, *m*-nitrotoluene, and *p*-nitrotoluene standards (>99.7% purity) and found to be completely linear. Enthalpy was standardized on melting of indium (a Perkin−Elmer standard), and the calibration was verified through an agreement with low-temperature phase transitions of cyclohexane. The background was reconstructed from peak-free regions by fitting with polynomial curves of suitably high order. Averaging across a series of DSC scans then reduces the effect of the random variations in the background curvature on the peak area. Both transition enthalpy and entropy were determined by integration of the heat-flow peaks, the entropy after dividing by T for each point. The latter procedure makes an assumption that is only partially correct, viz. that the DSC peak width is occurring solely because of T_V varying according to a distribution of w in the sample. While undoubtedly there is a very small distribution in w across the sample, the double integration also improves the consistency of the data with respect to resolution between the premonitory and main transitions.

Synchrotron X-ray Powder Diffraction (SXPD). Data for the determination of the molar volume as a function of temperature were collected at the two-circle powder diffractometer equipped with helium-operated cryostat, installed at the BM1B beamline of ESRF in Grenoble. Argon-sealed sample in a glass capillary of 0.25 mm diameter was rotated in the X-ray beam of wavelength $\lambda = 0.48572$ Å calibrated on NIST standard silicon. The reflection intensity from a 111-oriented silicon crystal analyzer was registered with a NaI scintillation counter. Short isothermal scans were performed between 225 and 345 K over the narrow angular range of Bragg reflections 200,020,004 of the double-cell perovskite type. The *d*-values were obtained as Lorentzian peak maxima by least-squares fitting.

Neutron Powder Diffraction (NPD). Data were collected at temperatures 20, 280, 300, 320, and 340 K using the BT-1 32-detector neutron powder diffractometer at NIST, described at the website of the Center for Neutron Research, http://www.ncnr.nist.gov/. The sample temperature was controlled in a closed-He-cycle cryofurnace. The 20 K data set was obtained over the angular range 3−168° 2θ with a step size of 0.05°, using a Cu (311) monochromator with a 90° takeoff angle, $\lambda = 1.5402(2)$ Å, and in-pile collimation of 15 min of arc. All remaining data sets were recorded over the 1.3−166.3° 2θ interval with a step size of 0.05° using a Ge (311) monochromator with a 75° takeoff angle, $\lambda = 2.0783(2)$ Å, and in-pile collimation of 15 min of arc. Refinements of the crystal and magnetic structures were performed using the Rietveld method as implemented in the GSAS software suite.[16] Magnetic form factors were taken from ref 17. Peak shapes were modeled using a Thompson−Cox−Hastings pseudo-Voigt profile function,[18] with a correction for asymmetry arising from axial divergence.[19] The background was approximated using a 4th order Chebyschev polynomial.

Electronic Structure Calculations. The molecular orbital energy levels for isolated 5-coordinate species were estimated from calculations using the CAESAR (crystal and electronic structure analyzer)[20] software package, based on the EHTB (extended Hückel tight binding) method.[21] The parameters and exponents employed in the calculation are listed in Table 2.

Results

Synthesis. Because the added oxygen atoms w are being structurally accommodated in the R layer, large R atoms in $RBaFe_2O_{5+w}$ widen the nonstoichiometry range. For example, excess oxygen can be incorporated up to $w = 0.65$ when R = Sm, and up to $w = 0.80$ for R = Nd, at the oxygen pressure of 1 bar and 1000 °C.[14] In contrast, small R atoms

---

(14) Karen, P.; Woodward, P. M. *J. Mater. Chem.* **1999**, *9*, 789.

(15) Werner, P.-E. *The Computer Programme SCANPI 9*; Institute of Inorganic Chemistry, University of Stockholm: Stockholm, Sweden, 1992.

(16) Larson, A. C.; Von Dreele, R. B. *Los Alamos Natl. Lab. [Rep. LAUR]* **1994**, *86*, 748.

(17) Brown, P. J. Magnetic Form Factors. In *International Tables for Crystallography, Volume C*; Wilson, A. J. C., Reidel, D., Eds.; Holland: Dortrecht, 1992, pp 391−399.

(18) Thompson, P.; Cox, D. E.; Hastings, J. B. *J. Appl. Crystallogr.* **1987**, *20*, 79.

(19) Finger, L. W.; Cox, D. E.; Jephcoat, A. P. *J. Appl. Crystallogr.* **1994**, *27*, 892.

(20) Ren, J.; Liang, W.; Whangbo, M.-H. *Crystal and Electronic Structure Analysis Using CAESAR*; PrimeColor Software, Inc.: Cary, NC, 1998.

(21) Whangbo, M.-H.; Hoffmann, R. *J. Am. Chem. Soc.* **1978**, *100*, 6093.

Table 2. Atomic Orbital Energies and Orbital Coefficients Used in the Extended Hückel Calculations

atom	orbital	H_{ii} (eV)	ξ_1	c_1	ξ_2	c_2
Mn	4s	−9.75	0.97	1.00		
	4p	−5.89	0.97	1.00		
	3d	−11.67	5.15	0.5139	1.70	0.6929
Fe	4s	−9.10	1.90	1.00		
	4p	−5.32	1.90	1.00		
	3d	−12.60	5.35	0.5505	2.00	0.6260
Co	4s	−9.21	2.00	1.00		
	4p	−5.29	2.00	1.00		
	3d	−13.18	5.55	0.5679	2.10	0.6059
O	2s	−32.30	2.275	1.00		
	2p	−14.80	2.275	1.00		

permit only a limited degree of oxygen nonstoichiometry, as illustrated by $TbBaFe_2O_{5+w}$ where the upper limit of w is approximately 0.05 in equilibrium with the appropriate gas atmosphere at 1000 °C.[9] Therefore, on the basis of the relatively small size of Y^{3+}, one would expect a rather limited range of oxygen nonstoichiometry for $YBaFe_2O_{5+w}$. Accordingly, only compositions that are close to the ideal stoichiometry ($0 < w < 0.028$) could be synthesized. Furthermore, successful synthesis of a single-phase double-cell perovskite occurs within a narrow window of synthesis conditions, as illustrated in Table 1. Table 1 also details the consequences of extending the synthesis conditions outside of this window. Attempts to accommodate more oxygen at 1000 °C resulted in demixing of orthorhombic $YFeO_3$ ($a = 5.620$ Å, $b = 7.588$ Å, $c = 5.280$ Å) and formation of a cubic $(Y,Ba)FeO_{3-\delta}$ perovskite-type phase ($a = 3.916$ Å). An excess reduction at the same temperature yielded a green product containing divalent iron, which, however, could be completely reoxidized back into the silvery single-phase $YBaFe_2O_{5+w}$ by correcting the partial pressure of oxygen. Upon reduction at approximately 600 °C, samples that seemingly have a small negative w can be synthesized. However, magnetization and synchrotron X-ray diffraction experiments show that such samples contain increasing amounts of metallic iron in apparent equilibrium with the double-cell perovskite phase. The composition of the single-phase bulk sample, having $w = 0.001$, was the first one within the homogeneity range.

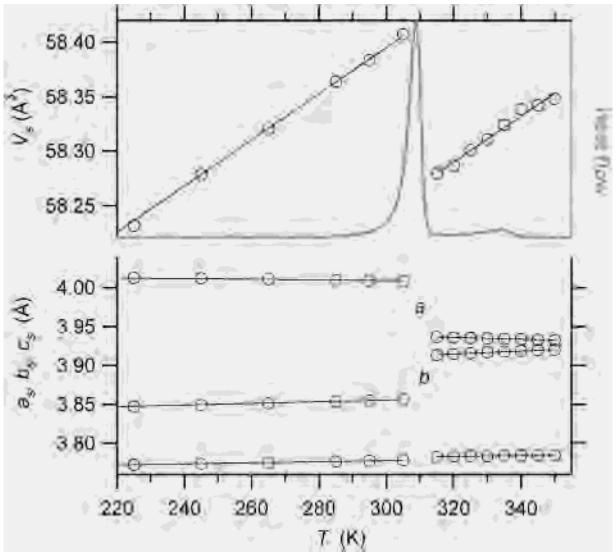

Figure 1. Unit cell data of $YBaFe_2O_{4.992}$ (derived from SXPD) referring to a single-perovskite type subcell compared with the DSC trace illustrating the caloric effects of the main (~308 K) and premonitory (~335 K) Verwey transition.

Table 3. Thermodynamics of the Successive Valence-Mixing Transitions upon Heating $YBaFe_2O_5$

transition:	class-I MV to class-II MV	class-II MV to class-III MV
T_V (in K; peak value)	309.5(3)	334.2(3)
ΔV (Jbar^{-1}mol^{-1})	−0.018(1)	not discernible
ΔH (kJ mol^{-1})	2.62(3)	0.150(8)
ΔS (Jmol^{-1}K^{-1})	8.51(9)	0.454(24)
T_V (in K; peak-center value[a])	307(6)	330(35)
dP/dT_V[b] (bar K^{-1})	−465(43)	not applicable

[a] As given by $T = \Delta H/\Delta S$. [b] From Clapeyron equation.

Localization of the MV Transitions. Two thermal effects are apparent on the DSC curves of $YBaFe_2O_{5+w}$ in Figure 1. As it is the case for other $RBaFe_2O_5$ phases, the strong endothermic peak (here at 308 K) refers to the transition from the class-I MV phase (charge-ordered) to the class-II MV phase (partially charge-separated), and the weak peak (334 K) manifests the completion of the valence mixing into the high-temperature, class-III MV phase. The unit-cell data show that the ordering of Fe^{2+} and Fe^{3+} upon cooling through the main transition is accomplished via a profound increase in the molar volume and orthorhombic distortion. The latter allows the Fe^{2+} square-pyramidal coordination to expand in the direction of the longer orthorhombic axis so that a long-range order of the two iron valence states occurs.[9] The weak transition, however, shows no abrupt unit-cell change. Only a minute orthorhombic distortion persists through this weak transition separating the class-II and class-III MV states. The origin of this slight orthorhombic distortion lies in the reduction of symmetry that arises because of the AFM ordering, and it accordingly disappears above T_N, (above some 400 K in general for various R) where the ideal tetragonal symmetry is restored.[9] The lack of long-range charge order in the intermediate class-II MV phase prevents extraction of the local iron coordination environment from the diffraction data. However, examination of the (electric) ligand-field gradients obtained from Mössbauer spectra[9] shows that the same charge-ordering mechanism applies for both the premonitory and the main Verwey transition. Namely, a uniaxial extension of one square-pyramidal base accompanied by squeezing a neighboring base. The difference between these two transitions is that the orthorhombic distortion needed for the premonitory transition originates in magnetostriction due to the AFM arrangement.[9]

The standard transition enthalpies and entropies are listed in Table 3 as obtained by averaging DSC-based data for several samples (the data were practically independent of the small variations in the oxygen content), and their signs correspond to a charge freezing/melting model. Comparison with other R variants reported previously in refs 11 (R = Nd and Sm) 22 (Gd) and 9 (Tb) shows the thermal effect being highest for $YBaFe_2O_5$. Even so, the value per iron atom is just about three-quarters of the ideal value of $R \ln 2 = 5.76$ J mol^{-1} K^{-1} suggested by Verwey et al.[23] for a full

---

(22) Karen, P. *J. Solid State Chem.* **2003**, *170*, 9.

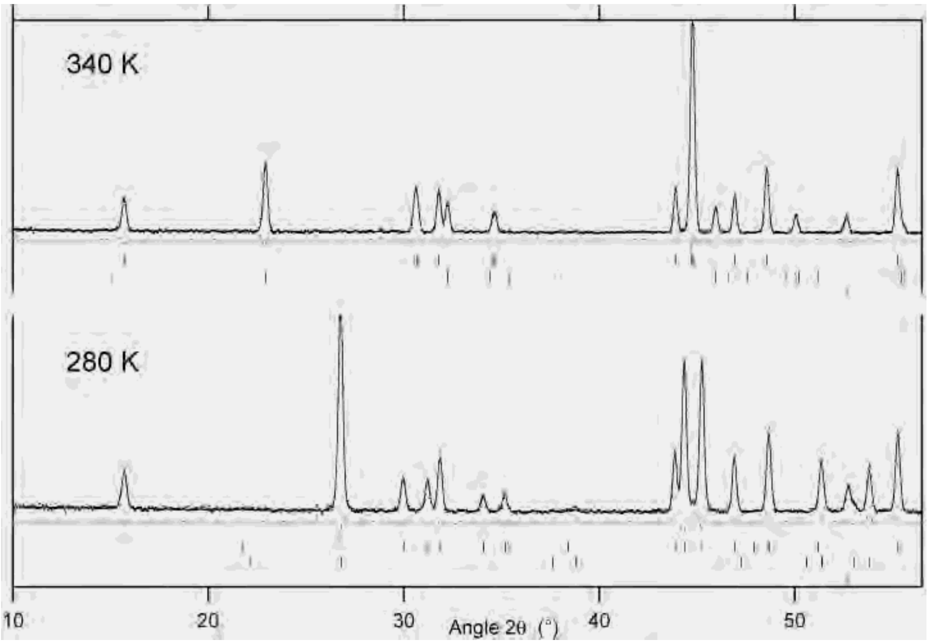

Figure 2. Detail of the observed (dots), calculated, and difference patterns obtained from the Rietveld structure refinement of the NPD data of the class-I (280 K) and class-III (340 K) MV phase of $YBaFe_2O_5$. The upper set of the vertical bars denotes the positions of the nuclear reflections, the middle set corresponds to the nonzero magnetic reflections, and the lower set refers to aluminum peaks from the cryofurnace.

ordering into the integer iron valences. The discrepancy could be due to contributions from changes in the magnetic order, but it also may be indicative of a residual valence mixing in the low-temperature charge-ordered phase. Given the low electrical conductivity, rather different coordination environments, and Mössbauer isomer shifts typical of the integer valences in this phase,[9] we believe that the assignment of this phase as a class-I MV signifies appropriately the effect of the two successive phase transitions that lead to its formation.

Nuclear and Magnetic Structures. NPD data sets of $YBaFe_2O_5$ collected at 20, 280, and 300 K correspond to the class-I MV phase (a charge-ordered structure). The next temperature of 320 K was purposely selected to fall into the existence range of the class-II MV phase, and finally, the 340 K data collection probes the class-III MV phase. Previous NPD studies on the related compound $TbBaFe_2O_5$ revealed a rearrangement in the magnetic structure that accompanies the charge ordering. The magnetic order changes from a $YBaFeCuO_5$-type arrangement above the main Verwey transition temperature (T_V) to a Wollan–Koehler[24] G-type magnetic structure below T_V.[9] Inspection of the $YBaFe_2O_5$ NPD patterns leaves little doubt that a magnetic phase transition does indeed take place between 300 and 320 K, as expected. Rietveld refinements were carried out using the appropriate structures of the MV class-I or class-III $TbBaFe_2O_5$ phases as starting models. Both models were tried for the 320 K data set where the class-II MV phase occurs, but the charge-ordered model did not provide statistically significant improvement in the fit to the data. Thus, we conclude that even though two signals can be detected in the Mössbauer data, long-range crystallographic charge order is not present above T_V in the class-II MV phase. Table 4 contains the results of the structural refinements. Figure 2 shows the Rietveld refinement profiles at 280 and 340 K. From the comparison of the low-angle region of these two diffraction patterns, it is easy to see the appearance of new magnetic Bragg peaks and the pronounced orthorhombic distortion exhibited by the class-I MV (charge-ordered) structure as compared with class-III MV state. Figures 3 and 4 illustrate the crystal and magnetic structures of these two phases. The refined atomic parameters show that in the class-III MV phase (340 K) there is a single crystallographic site for iron, and the local environment about each iron is a symmetric square-pyramidal coordination. In the class-I MV phase (at 20 K), the Fe^{3+} site retains a fairly symmetric coordination environment, although a shift of the Fe^{3+} ion toward the apex of the square pyramid leads to a contraction of the apical Fe–O distance. In contrast, the Fe^{2+} site becomes very distorted because of primarily a lengthening of the Fe–O(3) bonds. The change in magnetic structure is analogous to the transition already observed in $TbBaFe_2O_5$ in ref 9 and involves a switch from FM (in class-III MV) to AFM (in class-I MV) coupling between two iron atoms across the yttrium layer. The refinements of the class-I MV (charge-ordered) structure clearly distinguish the two valence states of iron. This follows directly from the distinct coordination environments of the two iron sites, which produce changes in the intensities of certain Bragg reflections and the appearance of superstructure lines in the charge-ordered state. However, the magnetic PND reflections do not carry the same clear distinction. Refinements of two separate magnetic moments at the charge-ordered di- and trivalent iron sites proved elusive both because of the weakness of the differential scattering contribution and

---

(23) Verwey, E. J. W.; Haayman, P. W.; Romeijn, F. C. *J. Chem. Phys.* **1947**, *15*, 181.
(24) Wollan, E. O.; Koehler, W. C. *Phys. Rev.* **1955**, *100*, 545.

Table 4. $YBaFe_2O_5$ Structure Refinement Results from NPD Data

T (K):	20	280	300	320	340
λ (Å)	1.5402	2.0783	2.0783	2.0783	2.0783
R_{wp}	0.0671	0.0789	0.0907	0.0783	0.0748
χ^2	4.78	1.38	1.91	1.25	1.17
space group	$Pmma^a$	$Pmma^a$	$Pmma^a$	$Pmmm^b$	$Pmmm^b$
a (Å)	8.0251(1)	8.0162(2)	8.0141(2)	3.93329(7)	3.93181(7)
b (Å)	3.83834(6)	3.85238(7)	3.85511(9)	3.91342(7)	3.91717(7)
c (Å)	7.5312(1)	7.5541(2)	7.5577(2)	7.5652(1)	7.5683(1)
$a_s - b_s$(Å)^c	0.1742	0.1557	0.1520	0.0199	0.0146
V (Å^3)	231.983(8)	233.28(1)	233.49(1)	116.447(5)	116.563(5)
Fe(1) z	0.2542(4)	0.2568(9)	0.257(1)	0.2640(2)	0.2641(2)
Fe(2) z	0.2695(4)	0.2662(9)	0.265(1)		
O(1) z	0.003(1)	0.001(3)	0.000(3)	0	0
O(2a) z	0.3213(7)	0.324(2)	0.325(2)	0.3137(5)	0.3140(6)
O(2b) z	0.3132(7)	0.307(2)	0.308(2)		
O(3) x	0.0098(7)	0.012(1)	0.011(2)	0	0
O(3) z	0.3119(3)	0.3130(4)	0.3115(4)	0.3127(5)	0.3125(6)
Y U_{iso} (Å^2)	0.0063(4)	0.0123(9)	0.013(1)	0.0152(8)	0.0137(7)
Ba U_{iso} (Å^2)	0.0039(6)	0.014(1)	0.017(1)	0.017(1)	0.0144(9)
Fe U_{iso}/U_{eqv} (Å^2)^{d,e}	0.0039(3)	0.0124(6)	0.0139(8)	0.0132	0.0122
O(1) U_{eqv} (Å^2)^d	0.0080	0.0138	0.0159	0.0181	0.0136
O(2) U_{eqv} (Å^2)^{d,f}	0.0065	0.0123	0.0129	0.0186	0.0188
O(3) U_{eqv} (Å^2)^d	0.0078	0.0128	0.0141	0.0146	0.0138
Fe M_y (μ_B)	3.82(2)	3.41(3)	3.26(3)	2.88(2)	2.76(2)
Fe M_z (μ_B)	0	0	0	−0.17(8)	−0.20(8)
Fe M_{Total} (μ_B)	3.82(2)	3.41(3)	3.26(3)	2.89(2)	2.77(2)

[a] Wyckoff positions for space group *Pmma* (nuclear cell) are: Ba at 2a (0,0,0); Y at 2c $(0,0,{}^1/_2)$; Fe(1) and O(1) at 2f $({}^1/_4,{}^1/_2,z)$; Fe(2) at 2f $({}^3/_4,{}^1/_2,z)$; O(2a) at 2e $({}^3/_4,0,z)$; O(2b) at 2e $({}^1/_4,0,z)$; O(3) at 4j $(x,{}^1/_2,z)$. [b] Wyckoff positions for space group *Pmmm* (nuclear cell) are: Ba at 1a (0,0,0); Y at 1c $(0,0,{}^1/_2)$; Fe at 2t $({}^1/_2,{}^1/_2,z)$; O(1) at 1f $({}^1/_2,{}^1/_2,0)$; O(2) at 2s $({}^1/_2,0,z)$; O(3) at 2r $(0,{}^1/_2,z)$. [c] Orthorhombic distortion; refers to the single-perovskite-type subcell. [d] U_{eqv} values are given for those atoms where anisotropic displacement parameters were used in the refinement. The U_{eqv} values are defined as one-third the trace of the diagonal matrix describing the shape of the thermal ellipsoid. A complete list of the anisotropic displacement parameters is given in the Supporting Information. [e] The displacement parameters for Fe(1) and Fe(2) were constrained to be equal. An isotropic displacement parameter was used in the charge-ordered state; anisotropic displacement parameters were used for the MV state. [f] The displacement parameters for O(2a) and O(2b) were constrained to be equal.

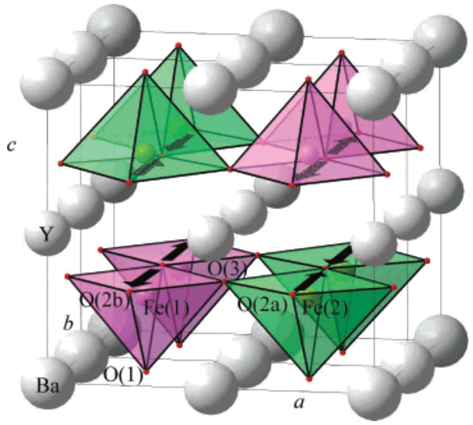

Figure 3. Crystal and magnetic structure of the class-I MV (charge-ordered) $YBaFe_2O_5$ at 20 K. Magnetic unit cell ($a \times 2b \times c$) is drawn.

correlations with other parameters. The ensuing lack of improvement in figures of merit justified refining only one common magnetic moment for iron atoms. The thermal evolution of the magnitude of this moment corresponds to a Brillouin-type behavior, as near as can be ascertained from the relatively coarse spacing of points as a function of temperature.

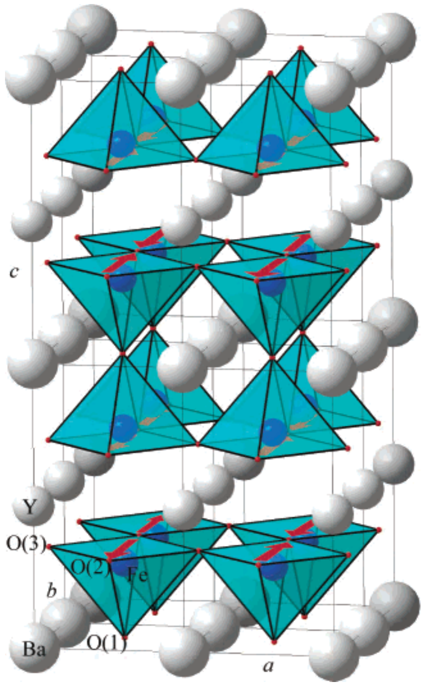

Figure 4. Crystal and magnetic structure of class-III MV (homogeneous-valence) $YBaFe_2O_5$ at 340 K. Note the FM interaction across the Y layer. Magnetic unit cell ($2a \times 2b \times 2c$) is drawn.

Discussion

Square-pyramidal coordination is a rather uncommon ligand environment for extended metal oxides. In rare instances, it is forced upon ions that normally adopt symmetric coordination environments, such as Li[25] and Mg,[26] by the preferred coordinations of other components in complex oxide structures. It is also formed upon addition of four ligands to a multiply bonded metal−oxygen group (ion), such as $VO^{(2+)}$ in calcium vanadium(IV) oxides[27] and other similar compounds of tetravalent vanadium. A trigonal bipyramid appears as the most commonly preferred alternative for pentacoordination. As noted by Gillespie,[28] the main domain where the square-pyramidal coordination has a chance to prevail over this alternative is in the various d-orbital fillings of transition metals. Typical square-pyramidal coordinators are the $3d^4$ and $3d^9$ ions with strong Jahn−Teller distortion removing the degeneracy of the e_g orbitals. Examples for Mn^{3+} in solely such coordination include $A_2Mn_2O_5$ (A = Ca[29] or Sr[30]); examples for Cu^{2+} are $La_2Cu_2O_5$[31] and the green Y_2BaCuO_5[32] phase. None of these explanations can be invoked to rationalize the square-pyramidal coordination in the double-cell perovskites containing iron or cobalt. Rather, the square-pyramidal coordination is imposed upon the transition metal ions as a

---

(25) Czekalla, R.; Jeitschko, W. *Z. Anorg. Allg. Chem.* **1993**, *619*, 2038.

(26) Tahiri, A. A.; El-Bali, B.; Lachkar, M.; Ouarsal, R.; Zavalij, P. Y. *Acta Crystallogr., Sect. E* **2002**, *58*, i9.

(27) Bouloux, J. C.; Galy, J. *J. Solid State Chem.* **1976**, *16*, 385.

(28) Gillespie, R. J. *J. Chem. Soc.* **1963**, 4679.

(29) Poeppelmeier, K. R.; Leonowicz, M. E.; Scanlon, J. C.; Longo, J. M.; Yelon, W. B. *J. Solid State Chem.* **1982**, *45*, 71.

(30) Caignaert, V.; Nguyen, N.; Hervieu, M.; Raveau, B. *Mater. Res. Bull.* **1985**, *20*, 479.

(31) La Placa, S. J.; Bringley, J. F.; Scott, B. A. *Acta Crystallogr., Sect. C* **1993**, *49*, 1415.

(32) Michel, C.; Raveau, B. *J. Solid State Chem.* **1982**, *43*, 73.

Table 5. Structural Information and Phase Transition Behavior for $YBaM_2O_5$ Double-Cell Perovskites

	$YBaMn_2O_5$	$YBaFe_2O_5$	$YBaCo_2O_5$
T_V (K)	>300	308	220
T_N (K)		430	330
T_C (K)	165		
Class-III MV phase		at 340 K	at 300 K
a (Å)		3.93193(7)	3.8922
b (Å)		3.91709(7)	3.8850
c/2 (Å)		3.7841(1)	3.7404
M−O distances (Å)		1 × 1.998(1)	1 × 1.934(3)
		2 × 1.995(1)	2 × 1.986(2)
		2 × 2.001(1)	2 × 1.983(1)
M−M distance (Å)		3.573	3.578
bond-valence sums			
Y		2.73	2.85
Ba		2.00	2.19
M		2.53	2.33
O		2.08, 1.93, 1.93	2.18, 1.89, 1.88
magnetic structure type		$YBaCuFeO_5$	G
Class-I MV phase	at 1.5 K	at 20 K	at 50 K
M^{2+}/M^{3+} arrangement	Figure 5a	Figure 5b	Figure 5b
a/2 (Å)	3.9145	4.0126(6)	3.9118(1)
b (Å)	3.9145	3.83834(6)	3.8746(1)
c/2 (Å)	3.8076	3.7656(1)	3.7184(1)
M^{2+}−O distance (Å)	1 × 1.961(9)	1 × 2.052(8)	1 × 2.06(2)
	4 × 2.086(5)	2 × 1.959(1)	2 × 1.955(2)
		2 × 2.109(6)	2 × 2.096(5)
M^{3+}−O distance (Å)	1 × 2.081(9)	1 × 1.891(8)	1 × 1.78(2)
	4 × 1.908(4)	2 × 1.970(2)	2 × 2.004(4)
		2 × 1.976(6)	2 × 1.894(5)
M−M distance (Å)	3.573	3.587	3.599
bond-valence sums			
Y	2.81	2.79	2.85
Ba	1.96	2.01	2.21
M	2.43, 3.10	2.23, 2.94	2.02, 2.69
O	2.13, 2.04	2.18, 1.97, 1.98, 1.92	2.26, 1.82, 1.93, 1.88
magnetic structure type	G	G	G

consequence of the layered ordering of R^{3+} and Ba^{2+}. To attain suitable coordination environments for both ions, oxygens are preferentially removed from the rare-earth layer, reducing the coordination number of R from 12 to 8. The oxygen-vacancy ordering is accompanied by a relaxation of the basal-plane oxygens toward the R ion. In this way, the transition metal ions are stabilized in an atypical coordination environment. An important aspect of this delicate structural balance is the R^{3+}, Ba^{2+} charge imbalance that results in the half-integer oxidation state for the transition metal ion, $M^{2.5+}$ in $RBaM_2O_5$. This combination of an unusual coordination environment and an unstable oxidation state for the transition metal ion is responsible for the remarkable phase transitions exhibited by these compounds.

Table 5 summarizes the phase transitions, relevant bond distances, bond valence sums, and magnetic behavior of $YBaM_2O_5$ (M = Mn, Fe, Co). Unfortunately, the valence-mixing temperature and structural information from the eventual class-III MV state are not known for $YBaMn_2O_5$ which is charge ordered at all temperatures investigated so far. Structural parameters for this compound in this hypothetical homogeneous (class-III) MV state can be estimated by averaging the Mn^{2+}−O and Mn^{3+}−O distances in the class-I MV state. From a purely structural viewpoint, the most significant change in $YBaM_2O_5$ upon progressing from Mn to Fe and onto Co is a contraction of the apical M−O bonds of the square-pyramidal coordination environment. The basal M−O bonds as well as the M−M distances across the Y^{3+} layer remain fairly constant. Figure 5 shows the charge-ordered structures of $YBaM_2O_5$. The charge-ordered arrangement of the di- and trivalent ions in $YBaMn_2O_5$ fulfills the Anderson charge-ordering condition[33] whereas it does not in $YBaFe_2O_5$ and $YBaCo_2O_5$. Instead of having all aliovalent neighbors, the respective isovalent iron and cobalt atoms arrange themselves in chains. Because such an arrangement is less stable electrostatically, it must be stabilized by the prevailing patterns of the orbital (and/or magnetic) ordering. Whereas for Mn^{2+} and Mn^{3+} a nearly isometric shape of the (semi-)filled d-orbital shell occurs, one of the x-shaped pseudo-t_{2g} orbitals is doubly occupied for Fe^{2+}. Indeed, stacking of these Fe^{2+} d_{xz} orbitals along the shorter *b* axis would explain the charge-ordering pattern. Alternative stacking of d_{yz} or d_{xy} would be disfavored by the slight magne-

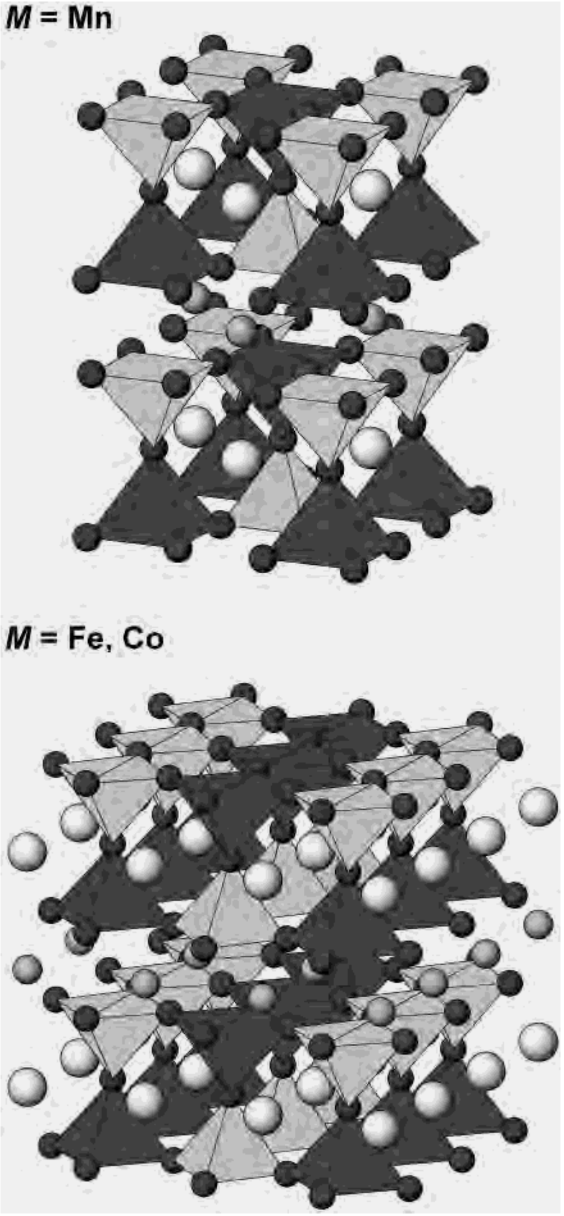

Figure 5. Ordering patterns of di- and trivalent ions in $YBaM_2O_5$ (M = Mn, Fe, Co).

---

(33) Anderson, P. W. *Phys. Rev.* **1956**, *102*, 1008.

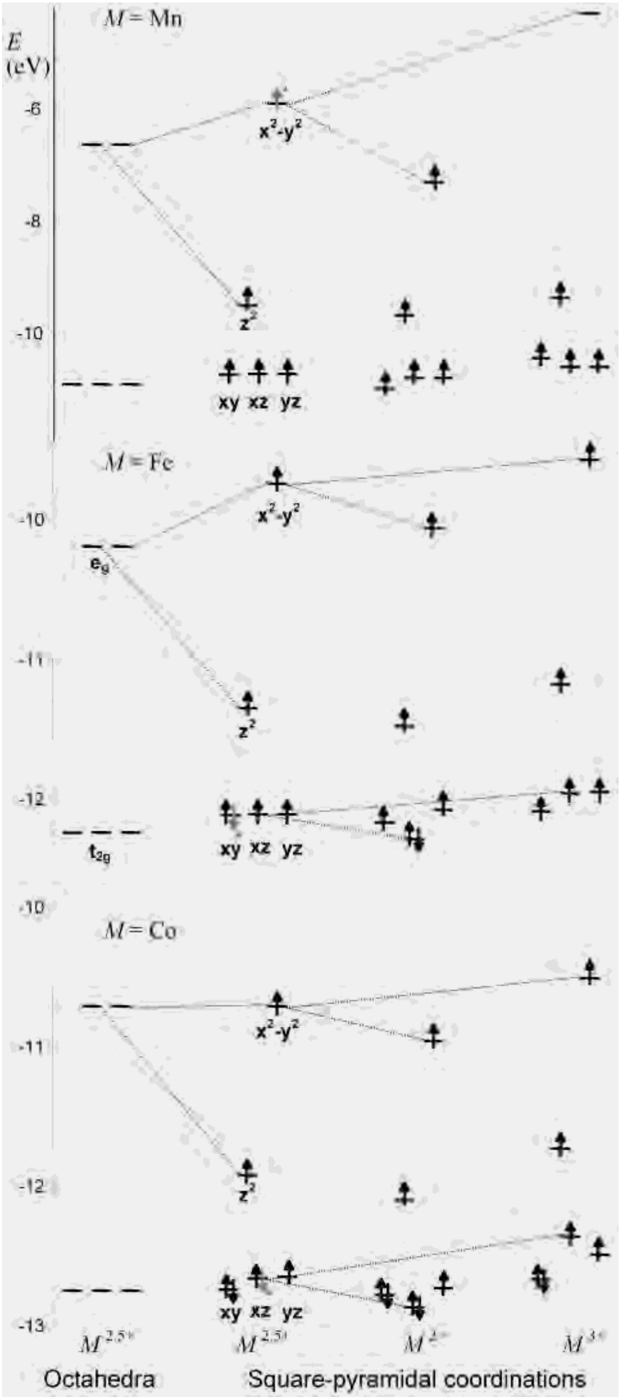

Figure 6. Energy levels of the d-orbitals in $YBaM_2O_5$ estimated using extended Hückel tight-binding calculations. Atomic coordinates used: M = Mn (2 and 300 K),[12] M = Fe (20 and 320 K) present data, M = Co (25 and 300 K).[13] The geometry of the hypothetical $Mn^{2.5+}$ square pyramid was extracted from the 300 K structure given in ref 12 by averaging Mn^{3+} and Mn^{2+} coordination environments.

tostrictive contraction along *b* existing already in the class-III MV state. In the cobalt case, two pseudo-t_{2g} orbitals of Co^{2+} and one of Co^{3+} are doubly occupied. The stacking of a doubly occupied Co^{2+} d_{xz} orbital would lead to the same orbital-ordering pattern provided Co^{3+} d_{xz} is singly occupied.

The distortions that occur upon entering the charge-ordered (class-I MV) state can be translated into the corresponding ligand-field splitting patterns and rationalized for the three M ions in question in $YBaM_2O_5$. Extended Hückel calculations were performed on isolated, five-coordinate, M-centered polyhedra. The geometry of these polyhedra was defined to match the coordination environments seen in experimentally determined crystal structures. For comparison, calculations were carried out for a symmetric octahedral coordination whose size was selected so as to satisfy the bond-valence condition of 2.5 valence units at M. The results are shown in Figure 6. Orbital occupancies are assumed to follow directly from the d-electron count, assuming high-spin configurations. Magnetic moments obtained from NPD analyses support this assumption. The first point to note is the crystal-field splitting in the class-III MV state and how the square-pyramidal coordination compares to the familiar octahedral crystal-field splitting. The d_{xy}, d_{xz}, and d_{yz} orbitals are nearly degenerate in energy, while the d_{z^2} orbital lies somewhat higher and the $d_{x^2-y^2}$ orbital lies considerably higher in energy. With respect to octahedral coordination, the main difference is a significant stabilization of the d_{z^2} orbital, and a somewhat smaller destabilization of the $d_{x^2-y^2}$ orbital. The structural distortions that accompany the transition from the class-III to the class-I MV state correlate with specific differences in orbital occupancies of the divalent and trivalent ions. For example, in the manganese−oxygen framework of $YBaMn_2O_5$, the effectively antibonding Mn $d_{x^2-y^2}$ orbital is singly occupied on Mn^{2+} but empty for Mn^{3+}. To lower the energy of the occupied Mn^{2+} $d_{x^2-y^2}$ orbital, a symmetric expansion of the $Mn^{2+}-O$ distances in the basal plane of the square pyramid occurs upon entering the charge-ordered state (class-I MV). In $YBaFe_2O_5$, the effectively antibonding Fe d_{xz} orbital is doubly occupied on Fe^{2+}, but only singly occupied on Fe^{3+}. The stabilization of the d_{xz} Fe^{2+} orbital follows directly from the expansion of two out of four $Fe^{2+}-O$ bonds in the basal plane of the square pyramid (the two bonds whose major component lies in the *x*-direction), as well as the expansion of the apical $Fe^{2+}-O$ bond. The polyhedral distortions that occur upon entering the charge-ordered state can be thought of as CJTD, which arise through asymmetric filling of the d-orbitals. Although in the strictest sense they are not Jahn−Teller distortions because the competing orbitals are not truly degenerate, they can still be described in terms of a 2nd order Jahn−Teller distortion. By almost any measure, the CJTD that occur in these materials are large. Similar behavior is observed in a number of transition metal perovskites where the e_g orbital set is either one-quarter filled, such as $LaMnO_3$,[34,35] or three-quarters filled, such as $KCuF_3$,[36] Ba_2CuWO_6,[37] or La_2CuSnO_6.[38] In contrast, partial filling of the t_{2g} orbital set, as found in $LaTiO_3$,[39,40] $LaVO_3$,[41] and $KFeF_3$,[42] does not typically lead to pronounced cooperative distortions of the

---

(34) Norby, P.; Kregh Andersen, I. G.; Kregh Andersen, E.; Andersen, N. H. *J. Solid State Chem.* **1995**, *119*, 191.
(35) Rodríguez-Carvajal, J.; Hennion, M.; Moussa, F.; Moudden, A. H.; Pinsard, L.; Revcolevschi, A. *Phys. Rev. B* **1998**, *57*, R3189.
(36) Burns, P. C.; Hawthorne, F. C.; Hofmeister, A. M.; Moret, S. L. *Phys. Chem. Miner.* **1996**, *23*, 141.
(37) García-Ruiz, A.; Bokhimi; Portilla, M. *J. Mater. Res.* **1992**, *7*, 24.
(38) Anderson, M. T.; Poeppelmeier, K. R. *Chem. Mater.* **1991**, *3*, 476.
(39) Eitel, M.; Greedan, J. E. *J. Less-Common Met.* **1986**, *116*, 95.
(40) Arao, M.; Inoue, Y.; Koyama, Y. *J. Phys. Chem. Solids* **2002**, *63*, 995.

octahedra. Taken in this context, we can say that the magnitude and stability of the CJTD in $YBaMn_2O_5$ is in line with conventional expectations, but its strength seen in $YBaCo_2O_5$ and particularly $YBaFe_2O_5$ suggests orbital ordering.

The magnetic properties of these compounds also show similarities and differences. In the low-temperature charge-ordered state, all three compounds adopt the same G-type magnetic structure where both the M−O−M superexchange and the M−M direct exchange interactions (across the Y^{3+} layer) are AFM. Normally, in insulating transition metal oxides of the perovskite-type, the e_g superexchange interactions control the nearest-neighbor magnetic coupling. The presence of half-filled d_{z^2} and $d_{x^2-y^2}$ orbitals in the case of $YBaFe_2O_5$ and $YBaCo_2O_5$ is consistent with the observation of the G-type AFM structure. However, consideration of the orbital filling and application of the Goodenough−Kanamori superexchange rules in the case of $YBaMn_2O_5$ leads to the conclusion that an A-type AFM structure (FM coupling to nearest neighbors in the *xy*-plane and AFM coupling in the *z*-direction)[24] should be favored. As suggested previously,[12] the observation of a G-type AFM structure can perhaps be attributed to the nonlinear Mn−O−Mn bonds, which allow mixing of $d_{x^2-y^2}$ and d_{xy} orbitals. It is also interesting to compare the coupling between the magnetic order and charge order. In the case of $YBaMn_2O_5$, the relationship $T_V > T_N$ implies that charge ordering is more stable than magnetic ordering. In $YBaFe_2O_5$ and $YBaCo_2O_5$, the opposite relationship is observed. However, the charge localization has more dramatic consequences in the iron-based phase where it is accompanied by a reversal (FM to AFM) of the direct-exchange coupling across the R layer.

To complete our comparison of the $YBaM_2O_5$ (M = Mn, Fe, Co) phases, let us consider the stability of the charge-ordered (type I-MV) states. In a first approximation, take note of the differences in Figure 6 between the occupied orbitals of the class-III and class-I ions. It is clearly to be expected that the charge-ordered state in $YBaMn_2O_5$ is considerably more stable than for the Fe and Co variants. This seems to agree with the experimental evidence. The charge-ordering temperature of $YBaMn_2O_5$ is not known beyond the fact that charge ordering is strongly established at room temperature. The comparison between $YBaFe_2O_5$ and $YBaCo_2O_5$ is too delicate within the approximations of Figure 6 and must be aided by experimental evidence. The charge-ordering transition in $YBaFe_2O_5$ occurs at ~308 K, whereas $T_V \cong 220$ K for $YBaCo_2O_5$. For $YBaFe_2O_5$, the transition is clearly of the first order and is accompanied by a pronounced expansion along *a*, typical of the d_{xz} orbital ordering. In $YBaCo_2O_5$, it has characteristics of a second (or higher) order transition, and although the Co−O bond distances do undergo significant changes (primarily as a result of displacements of the cobalt ions either toward or away from the apical oxygen), the transition produces a much smaller orthorhombic distortion of the unit cell. Charge ordering is accompanied by a rearrangement of the AFM structure in $YBaFe_2O_5$, but not in $YBaCo_2O_5$. When the experimental evidence is considered collectively, there can be little doubt that the charge-ordered state is more stable in $YBaFe_2O_5$ than it is in $YBaCo_2O_5$. This is likely to reflect the ambiguity of ordering three doubly occupied orbitals per two Co atoms, as compared with the simple scheme of stacking the Fe^{2+} d_{xz} orbitals within a sufficiently orthorhombically distorted structure.

Conclusions

Among the double-cell perovskite family $RBaFe_2O_5$ (R signifying a trivalent rare-earth ion), $YBaFe_2O_5$ has the narrowest range of phase stability with respect to the oxygen nonstoichiometry, but the most stable charge-ordered state reported to date. NPD and DSC have been used to show that $YBaFe_2O_5$ exhibits a succession of class-III, II, and I MV phases upon decreasing temperature. The transition from a class-II to a class-I MV state, which occurs at ~308 K, is particularly spectacular. A profound increase of the originally small magnetostrictive orthorhombic distortion creates space for a pronounced CJTD of the Fe^{2+} square pyramid that corresponds to ordering of the doubly occupied d_{xz} orbitals on the divalent iron site. The orbital ordering is evidenced from the orthorhombic distortion and estimates of the crystal field splitting. As a consequence, the Anderson charge-ordering condition of point charges is neither applicable nor fulfilled. Bond-valence analysis suggests a high degree of separation of the two iron valences, consistent with a very strong charge-ordering localization. Furthermore, a dramatic rearrangement of the AFM structure ensues, where a double-exchange FM interaction between two iron atoms facing each other in the class-III MV phase is replaced by an AFM coupling in the class-I MV phase. Experimental evidence suggests that the charge-ordered state of $YBaFe_2O_5$ is more stable than for $YBaCo_2O_5$, a feature that would seem to originate from the strong coupling between charge, orbital, and spin ordering in this compound.

Acknowledgment. We acknowledge the support of the National Institute of Standards and Technology, U.S. Department of Commerce, in providing the neutron research facilities used in this work. Furthermore, experimental assistance from the staff of the Swiss-Norwegian Beam Lines at ESRF is gratefully acknowledged.

Note Added after ASAP: The version of this paper posted ASAP on January 29, 2003, contained incorrect values in Table 3. The correct values are present in the version posted on February 6, 2003.

Supporting Information Available: CIF data for the class-I (charge-ordered) and class-III (valence-mixed) structures of $YBaFe_2O_5$ and a table of the refined anisotropic displacement parameters. This material is available free of charge via the Internet at http://pubs.acs.org.

IC026022Z

(41) Bordet, P.; Chaillout, C.; Marezio, M.; Huang, Q.; Santoro, A.; Cheong, S.-W.; Takagi, H.; Oglesby, C. S.; Batlogg, B. *J. Solid State Chem.* **1993**, *106*, 253.

(42) Miyata, N.; Tanaka, K.; Marumo, F. *Acta Crystallogr., Sect. B* **1983**, *39*, 561.